

Final Draft
of the original manuscript:

Kintzel, O.; Khan, S.; Mosler, J.:

**A novel isotropic quasi-brittle damage model applied to LCF
analyses of Al2024**

In: International Journal of Fatigue (2010) Elsevier

DOI: 10.1016/j.ijfatigue.2010.07.001

A novel isotropic quasi-brittle damage model applied to LCF analyses of Al2024

O. Kintzel^a, S. Khan^a, J. Mosler^{a,*}

^aGKSS Research Centre Geesthacht, Institute of Materials Research, Materials Mechanics, Max-Planck-Str. 1, 21502 Geesthacht, Germany

Abstract

The current paper deals with the assessment and the numerical simulation of low cycle fatigue of an aluminum 2024 alloy. According to experimental observations, the material response of Al2024 is highly direction-dependent showing a material behavior between ductile and brittle. In particular, in its corresponding (small transversal) S-direction, the material behavior can be characterized as quasi-brittle. For the modeling of such a mechanical response, a novel, fully coupled isotropic ductile-brittle continuum damage mechanics model is proposed. Since the resulting model shows a large number of material parameters, an efficient, hybrid parameter identification strategy is discussed. Within this strategy, as many parameters as possible have been determined a priori by exploiting analogies to established theories (like PARIS' law), while the remaining free unknowns are computed by solving an optimization problem. Comparisons between the experimentally observed and the numerically simulated lifetimes reveal the prediction capability of the proposed model.

Keywords: Aluminum alloys, Anisotropy, Damage mechanics, Ductile brittle transition, Plasticity, Low cycle fatigue

1. Introduction

High-performance materials like aluminum alloys are frequently employed in structural components of transportation vehicles (e.g., airplanes, automobiles and motorcycles). They have a high strength-to-weight-ratio and a high corrosion-resistance resulting in high efficiency. In particular, Al2024 is frequently used for components in the aerospace industry, e.g., for airframes or the fuselage of airplanes. This special aluminum alloy is known to be very damage tolerant and a good fatigue performer, cf. [1]. Due to practical relevance, the material properties of aluminum alloys have been analyzed extensively to assess their performance under single loading events (monotonic loading) as well as under repeated loading at low stress levels (high cycle fatigue (HCF)), cf. [1].

Engineering structures frequently made of high-strength alloys such as aerospace structures are usually subjected to a number of loading incidents during service life which are often of cyclic nature like recurrent landing operations or alternate pressure loadings at high altitudes. In benign situations, the stress levels are comparatively low. However, during critical overloads, e.g., experienced during unpredictable mechanical events like tough landing operations, bad weather conditions, etc., the material may experience higher local stresses. Even though the bulk of the material may be below the yield limit, local flaws or inhomogeneities may increase the local stress level above the elastic regime, which may promote material degradation at higher stress levels (low cycle fatigue (LCF)). Thus, the experimental assessment of the LCF behavior of aluminum alloys is of great importance. Usually, a number of experiments

have to be conducted under distinct loading conditions which is costly and time-consuming. The demand for numerical models for the simulation of LCF is, thus, obvious.

Evidently, the LCF behavior of aluminum alloys such as Al2024, or more precisely, their mechanical response in general, is strongly affected by the kind of manufacturing process. For instance, the thermomechanical treatment during wrought processing like hot working can produce highly directional grain structures and a significant degree of texturing. As a result, the material response may be direction-dependent. Recently, the material behavior in the longitudinal (L-), the transversal (T-) and the small transversal (S-) directions of a block of Al2024-T351 have been analyzed, cf. [10, 26]. In monotonic loading tests, the material response for specimens loaded in S-direction was less ductile and had a reduced rupture strain compared to those loaded in L- or T-directions. Moreover, in contrast to the L- and T-direction, necking was negligible and the final fracture surface was almost perpendicular to the loading direction. In summary, the material behavior in S-direction can be characterized as quasi-brittle, i.e., it lies in a certain range between ductile and brittle. Even though the underlying damage process is driven by local plastic strain accumulation as well, i.e., can be considered as ductile, the amount of global plastic deformation and the total energy absorbed is comparably small. The aforementioned quasi-brittle damage mechanism might also have a considerable effect on the damage process under LCF. Therefore, a novel material model capable of describing such a quasi-brittle damage is elaborated within the present paper. It is based on a new approach for brittle damage combined with a well-established model for ductile material degradation.

Models describing the failure processes in ductile materials, can be classified into two major groups: Micromechanically based models and those which approximate the respec-

*Corresponding author

Email address: joern.mosler@gkss.de (J. Mosler)

tive damage processes by means of rather phenomenological approaches. So-called *ductile fracture models* belong to the first class. They are based on (semi-) analytical homogenization procedures of void growth in representative volume elements, cf. [24, 3]. In the past, either coupled approaches [8, 22], where the softening behavior is simulated by means of a fully coupled elasto-plastic yield criterion, or uncoupled criteria [21], where failure is assumed when the evolution of the damage variable reaches a critical threshold, were used. In the last three decades, this modeling class has seen a rapid development. For the modeling of the monotonic loading behavior of Al2024 in S-direction, refer to [23]. Even though ductile fracture models can be quite general and may include rather complex void shapes or may consider damage accumulation under cyclic loading (see [11] and references therein), their (semi-) analytical tractability is naturally limited. In more recent analyses of material degradation, multiscale finite element approaches are thus used, cf. [25].

In the second class of models, the damage process is described by means of a more phenomenological approach. An explicit micro-mechanical modelling of defect evolution such as void growth in a representative volume element is not considered and no homogenization procedure is applied. Different to ductile fracture models, where the yield function depends on a softening variable, material degradation is taken into account by reducing the stored energy function, while the respective evolution equations are derived by considering certain general principles like the effective stress concept or the principle of strain equivalence [13] or energy equivalence [5]. Starting from the early proposition by KACHANOV [9] for ductile creep damage, this phenomenological approach has already been applied to a wide range of different mechanical problems with great success. Especially the ductile damage model of LEMAITRE [13] became very popular. It has been generalized to a fully anisotropic damage law in [15]. This modeling class is often referred to as *continuum damage mechanics (CDM)*.

Due to the complex microstructure of Al2024 (see [26, 10]), a micromechanically based model does not seem to be promising for analyzing the resulting LCF response. Instead, a phenomenological CDM approach is considered in the present paper. In our earlier analyses in the past, only ductile damage was taken into account, cf. [26, 10]. However, since the microstructural arrangement of Al2024, as observed in our current sample [20], may favor also brittle failure modes, a fully coupled model is proposed here. While ductile damage is modeled in a similar fashion as advocated in [13] (with few modifications), a novel approach is elaborated for brittle damage. In sharp contrast to the ductile damage model, material degradation can already evolve below the yield limit. Since early work on a large number of smooth and notched specimen demonstrated that wide variations in commercial aluminum alloys caused little or no detectable differences in fatigue strength [1], the novel coupled damage model is also applicable to a wider range of aluminum alloys.

The paper is structured as follows: In Section 2, the microstructure of Al2024-T351 is described. The micromechanisms associated with material damage are briefly explained in

Section 3. The novel CDM model is elaborated in Section 4. Based on mechanical experiments summarized in Section 5, the calibration of the CDM model to Al2024 is discussed in Section 6. Finally, the numerical simulations presented in Section 7 reveal the prediction capability of the novel quasi-brittle damage model for low cycle fatigue.

2. The microstructure of Al2024-T351

The material currently investigated is the aluminum alloy Al2024-T351. Typically, this material is used in thin sheets, e.g., for aircraft components. All specimens were cut from a block of Al2024 with a thickness of 100 mm.

The matrix is precipitation hardened by finely dispersed secondary phases Al_2Cu and Al_2CuMg [20]. The chemical composition is given in Tab. 1. Copper is the main alloying component. Manganese, together with magnesium, improves in particular the quenching properties and chromium enhances the corrosion resistance.

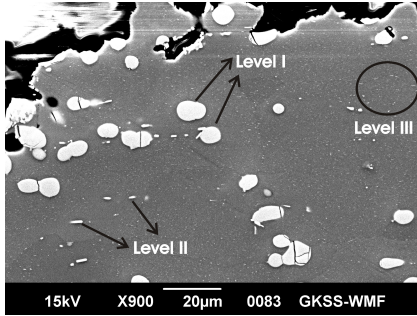
Table 1: Chemical composition of the considered AL2024 alloy (weight %)

Cu	Mg	Mn	Si	Fe	Cr	Al
4.11	1.12	0.46	0.048	0.05	0.003	Rest

The label T351 characterizes the wrought processing routine where T3 indicates solution heat treatment, air quenching and cold working, while 51 stands for stress relief by cold stretching. Before repeated rolling, the blocks are roughly 300-600 mm thick. Already after cooling down, the secondary phases are coarsely distributed throughout the Al-matrix. During hot rolling, particle clusters are formed (henceforth called particles of level I) aligned in rolling direction which form internal networks separating the structure into flat disks of Al-matrix domains surrounded by particle free bands (PFB). A confined recrystallization initiated during hot working leads to a texture with grain dimensions elongated in rolling direction. During solution heat treatment after hot working some coarse particles are dispersed into the Al-matrix favorably at grain boundaries (grain boundary segregation; henceforth labeled particles of level II) with precipitates-free zones (PFZ) around. During mild quenching in air, ageing occurs allowing a precipitation of fine particles into the Al-matrix (henceforth labeled as particles of level III) which hardens the alloy by acting as dispersoids or grain refining agents. To relieve residual stresses and to straighten the plate, it is work-hardened by stretching until a plastic deformation of 1.5-3% is reached.

Some words on microstructural dimensions (see Tab. 2): The network-like connected particle clusters of level I have a particle size of $23.5 \pm 16.7 \mu\text{m}$ and are surrounded by PFB of approximately $5 \mu\text{m}$ -thickness. The matrix domains are formed like disks with an average radius $236.5 \pm 125.5 \mu\text{m}$ and thickness of $26.3 \pm 11.3 \mu\text{m}$, hardened by secondary particles of level III with a particle size of $0.036 \pm 0.038 \mu\text{m}$. The particles of level III are finely distributed throughout the Al-matrix

and are shaped like small needles. The dispersoids and some external inclusions (oxides, etc.) of level II with a particle size of $0.30 \pm 0.21 \mu\text{m}$ are located at the grain boundaries. The grains are aligned in rolling direction and are formed in a pancake shape with an average width of $120 \mu\text{m}$ and an average thickness of $52 \mu\text{m}$.



Particle size	Mean diameter	Volume fraction
Level I	$23.5 \pm 16.7 \mu\text{m}$	$3.2 \pm 0.7 \%$
Level II	$0.30 \pm 0.21 \mu\text{m}$	$4.8 \pm 2.1 \%$
Level III	$0.036 \pm 0.038 \mu\text{m}$	$2.3 \pm 1.2 \%$

Table 2: Dimensions and volume fractions of the particles of level I, II and III, cf. [20]

3. Characterization of the microstructural failure modes

In the following, the failure modes under monotonic and cyclic loading are briefly discussed (see also [10]). To analyze the corresponding failure processes, tests on smooth and notched round bars (RB) were conducted in different loading directions as shown in Fig. 1. Experimental evidence in form of SEM pictures, which were taken from the fracture surfaces, is provided. With the aid of imaging software it was possible to produce also three-dimensional visualizations of the fracture surfaces for a better characterization of the failure mechanisms.

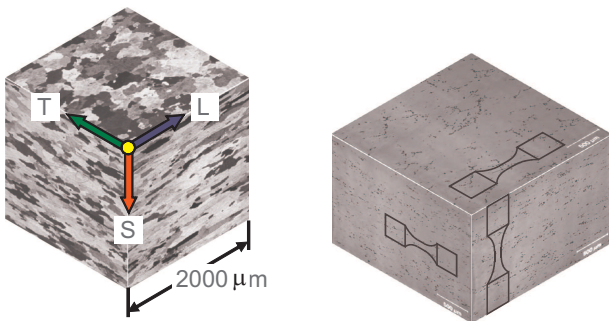


Figure 1: Characterization of S-, L- and T-directions and specimens taken

3.1. Monotonic loading

Monotonic uni-axial tensile tests on smooth round bars as presented in Fig. 2 revealed that the plastic deformation follows

the same characteristics in the beginning of the loading process in all tested directions. However, while the plastic behavior

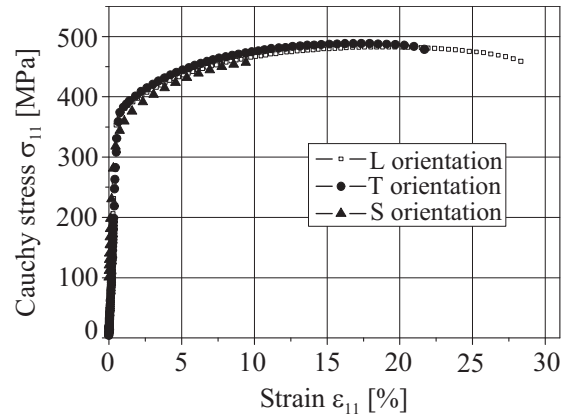


Figure 2: Stress-strain diagrams for uni-axial tension for smooth round bars

in L- and T-directions is nearly uniform even in the non-linear range, the ductility in S-direction is reduced and fracture occurs already very early. Furthermore, for specimens loaded in S-direction, necking was almost negligible and a flat-faced type fracture surface could be detected as illustrated in Fig. 3. In

Loading Direction	T	L	SL	S
Fracture surface orientation				

Figure 3: Fracture surface orientations for different loading directions

summary, for specimens loaded in L- or T-direction mostly a slant-shear fracture surface was observed and for specimens inclined with respect to the S-direction the fracture surface was flat-faced. Concluding, the overall plastic deformation is reduced in S-direction and the failure process is more brittle. More precisely, it can be characterized as quasi-brittle.

Fracture in commercial aluminum alloys is typically caused by microvoid formation at second-phase particles either by decohesion at the particle/matrix interfaces or by fracture of large and brittle intermetallic particles or coarse precipitates, sometimes also at smaller dispersoids and precipitates [23]. During coalescence, the rupture of the ligament, void impingement or shear rupture may follow. An important failure mode in aluminum alloys with a high amount of larger particles is void sheet coalescence by the process of linking up of smaller voids along bands of shear between larger voids, leading to premature void coalescence. Since larger constituents are prevalent in Al2024, which cannot be further resolved by heat treatment, the fracture toughness is generally reduced in aluminum alloys. The direction-dependent behavior can be explained by taking the softer PFB around the particle clusters of level I and

the softer PFZ near the grain boundaries (level II) into account, which are denuded zones devoid of particles (see [6]). They are preferential sites of localized plastic slip. For specimens loaded in L- and T-direction, damage may nucleate in the weakest part of the microstructure, the PFB, but has to cross the tougher matrix material leading to higher strength and dominant slant-shear fracture. By way of contrast, for specimens loaded in S-direction, the damage rate in the softer PFB is increased and the fracture process follows mode I along the interfaces between the PFB and particle clusters of level I (transgranular cleavage or quasi-cleavage) or the interfaces between the PFZ and the grain boundaries (intergranular separation). Since both microstructural features are preferentially oriented in rolling direction (direction of the long grain dimension), the fracture surface becomes flat-faced.

In Fig. 4, 3D-visualizations of the fracture surface for the L- and S-directions are presented. For the L-direction, the fracture process can be characterized as a dimple rupture, since the shear lips between the dimples and a rough surface structure are clearly visible. For the S-direction, the fracture surface is flat-faced with different height levels connected by walls of intense shear rupture (“shear lips”). As can be seen in Fig. 5, where a dimple structure can be observed for both loading directions, the primarily damage process is caused by ductile fracture, i.e., microvoid nucleation and coalescence. However, for the S-direction this is more localized in the softer precipitate free zones leading to a flat-faced fracture surface with less expenditure of overall energy.

3.2. Cyclic loading

The failure process in cyclic loading is different than that in monotonic loading. The plastic strain range is smaller, but for a high number of cycles, the accumulated plastic strain may exceed that of a corresponding monotonic loading test by far leading to intense plastic strain accumulation.

The damage process for cyclic loading can be divided into three regimes: In the first of those, the accumulation of plastic strain and the increase in dislocation density leads to a three-dimensional arrangement of slip bands. In the beginning, planar slip arrangements prevail where the dislocation movement is confined to local bundles or veins due to primary slip, until a three-dimensional cell structure is finally formed when secondary slip becomes more active. For higher load levels, the transformation to a cell-like structure occurs earlier which is also dependent on other intrinsic factors, cf. [1]. When an almost stable arrangement of dislocation structures is reached, a saturated cyclic stress-strain curve (CSS) is formed. For aluminum alloys in overaged conditions where the larger fraction of particles is incoherent and non-shearable, cyclic hardening instead of cyclic softening can be observed during saturation. The aforementioned process defines the initiation phase of damage. It bears emphasis that this phase can take up to one half or more of the total lifetime. In the second phase of the damage process, microcracks are initiated which may nucleate at microstructural stress raisers like voids, inclusions, grain boundaries, stronger second-phase particles or notches where the local stresses and plastic strains are concentrated, cf. [2, 12].

Finally, during the last phase, the microcracks, which are distributed over the structure, evolve to mesocracks forming eventually a dominant macrocrack which propagates until the structure fails.

For the definition of mesocrack initiation, the first stage of microcrack propagation is important. The crack initiation and propagation phase is typically divided into two stages. Within stage I, crack growth follows the direction of the maximum shear stress and nucleation starts typically at the surface where slip bands have produced intrusions and extrusions leading to a rough surface structure and micronotches generating stress concentrations. Subsequently, the crack growth changes to a direction perpendicular to the principal tensile stress direction. This is called stage II crack growth. Since this is usually correlated to macrocrack growth, only stage I is of interest for the prediction of mesocrack initiation. Roughly, a mesocrack is initiated, if a certain characteristic crack length is reached which is typically in the range of 0.5 to 1 mm. The duration of shear crack growth is longer, if the plastic strain is more localized or the stress range is higher. This is the case, if the structure contains coherent particles which are shearable (underaged condition), since they can be easily cut by dislocations and favor planar slip bands. For incoherent particles which are non-shearable (overaged condition), the dislocations cannot cross the particles such that the mean intercepts of the incoherent particles define the length of the active parts of the slip bands with fewer dislocations initiated, moving and piling-up against the obstacles leading to a higher overall fatigue resistance, cf. [1]. To the best knowledge of the authors, the current sample of Al2024 is in an overaged condition with a mixture of shearable and non-shearable particles which leads to good fatigue performance, since the plastic slip is more homogeneous. The softer PFB and PFZ are also regions of intense plastic strain localization and fatigue crack growth, but participate only, if the sample is loaded such that the particle-free interfaces are oriented in direction of maximum shear [1].

Microcrack growth initiates dominantly at the surface, since single slip leading to higher strain localization is more easily accommodated in surface grains than in constrained bulk grains where a large amount of multiple slip is necessary. In Fig. 6, a visualization of an initial mesocrack at the notch root of a notched round bar is presented. On the right-hand side of Fig. 6, it is visible that the particles of level I and II are partly broken and partly intact which shows that the sample has a mixed state of ageing. Concluding, the plastic strain accumulation, which is the primary ductile micromechanism, leads to plastic strain localization. Localized plastic slip may produce large slip offsets at the surface generating micronotches and microcracks. Any microstructural feature that results in an inhomogeneous plastic strain distribution leads to undesirable local stress concentrations at microstructural stress raisers. Such concentration sites could be the particle/matrix interfaces which can be clearly seen in Fig. 6 where the crack path follows the path between the fractured larger particles.

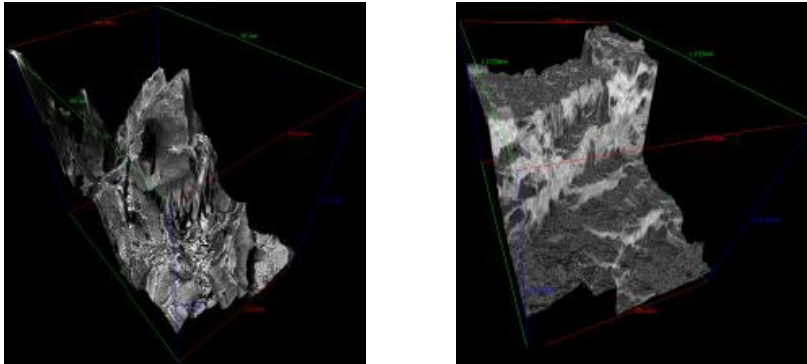


Figure 4: Monotonic loading. 3D-visualizations of the fracture surfaces for different loading conditions: a) L-direction; b) S-direction

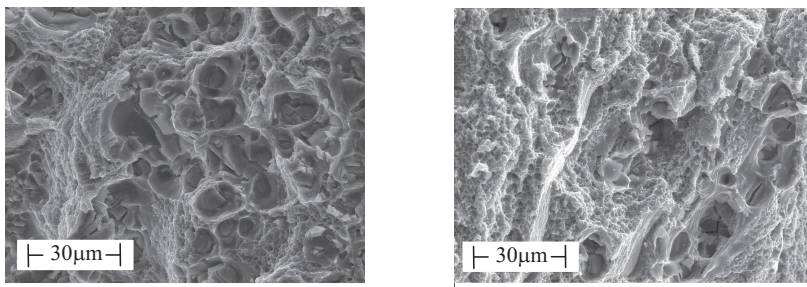


Figure 5: Monotonic loading; fracture surfaces: a) L-direction (ductile); b) S-direction (quasi-brittle)

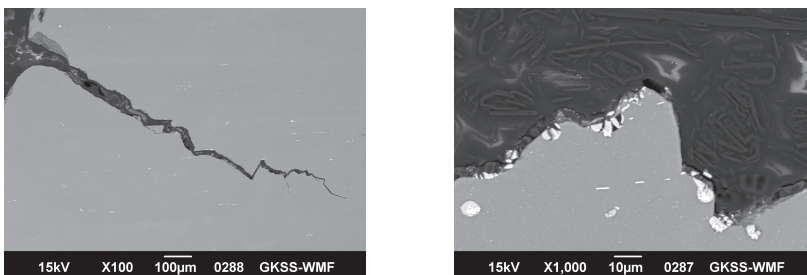


Figure 6: Cyclic loading. Lateral SEM micrographs of cyclically damaged notched specimens. a) Mesocrack initiation; b) Coherent and incoherent particles

3.3. Conclusion

In summary, the material behavior in S-direction can be characterized as quasi-brittle. More precisely, plastic strain accumulation as damage driving process as well as small fatigue crack growth as brittle damage mechanism can be observed for LCF. Therefore, a coupled ductile-brittle damage law seems to be promising. Such a model will be elaborated within the next section.

4. CDM material modeling

In the current section, a novel coupled ductile-brittle damage model suitable for the numerical analysis of LCF in aluminum alloys is outlined. For the ductile damage model, an evolution law is used which depends on the plastic strain rate and the energy release rate as proposed in LEMAITRE, cf. [13]. However, in contrast to the framework in [13], not only effective CAUCHY stresses but also effective hardening stresses are considered, cf. [7]. For the brittle damage accumulation, a novel damage indicator function is introduced which depends also on the energy release rate and thus, on the elasto-plastic strain accumulation. Its related damage evolution is controlled by the damage mechanism associated with fatigue crack growth. The introduction of a shift tensor, which plays a similar role as the back stress tensor in elasto-plasticity, allows the consideration of damage accumulation under cyclic loading.

This section is structured as follows: First, the ductile and the brittle damage models are introduced and explained in detail. Finally, they are combined to yield a fully coupled ductile-brittle damage law. Throughout the paper, a geometrically linear setting is used, where the strains are coupled additively according to

$$\boldsymbol{\epsilon} = \boldsymbol{\epsilon}^e + \boldsymbol{\epsilon}^p. \quad (1)$$

Here, $\boldsymbol{\epsilon}$ represents the total strains, and $\boldsymbol{\epsilon}^e$ and $\boldsymbol{\epsilon}^p$ are the elastic and the plastic parts of $\boldsymbol{\epsilon}$.

4.1. The ductile damage model

For describing typical plastic effects such as the BAUSCHINGER effect, cyclic hardening up to saturation as well to allow a good approximation of the plastic hysteresis curve (see [14], p. 234), three back stress tensors $\mathbf{Q}_k^{(j)}$, ($j=1,2,3$) and an isotropic hardening stress Q_i are introduced. With these assumptions, a HELMHOLTZ energy potential of the type

$$\rho \Psi^{ep} = \omega \left(\frac{\boldsymbol{\epsilon}^e : \mathbb{C} : \boldsymbol{\epsilon}^e}{2} + \sum_{j=1}^3 H_k^{(j)} \frac{\boldsymbol{\alpha}_k^{(j)} : \boldsymbol{\alpha}_k^{(j)}}{2} + H_i \frac{\alpha_i^2}{2} \right) \quad (2)$$

is adopted in what follows. Here, $\mathbb{C} = \kappa \mathbf{I} \otimes \mathbf{I} + 2\mu \mathbb{P}_{dev}$ is the isotropic elastic stiffness tensor involving the bulk and shear moduli κ and μ , respectively, H_i and H_k are hardening moduli and α_i and $\boldsymbol{\alpha}_k^{(j)}$ represent the strain-like dual variables to Q_i and $\mathbf{Q}_k^{(j)}$, respectively. $\omega = (1 - D)$ is the so-called *continuity function* which depends on the damage variable D . According to Eq. (2) and in contrast to [13], the complete stored energy function is reduced by ω which may lie in the range $[0,1]$.

Based on Eq. (2), the state variables can be derived in standard manner, i.e., by means of the gradients to the energy potential (2). More precisely,

$$\boldsymbol{\sigma} = \rho \frac{\partial \Psi^{ep}}{\partial \boldsymbol{\epsilon}^e} = -\rho \frac{\partial \Psi^{ep}}{\partial \boldsymbol{\epsilon}^p} = \omega \mathbb{C} : \boldsymbol{\epsilon}^e, \quad (3)$$

$$\mathbf{Q}_k^{(j)} = -\rho \frac{\partial \Psi^{ep}}{\partial \boldsymbol{\alpha}_k^{(j)}} = -\omega H_k^{(j)} \boldsymbol{\alpha}_k^{(j)} \quad (j = 1, 2, 3), \quad (4)$$

$$Q_i = -\rho \frac{\partial \Psi^{ep}}{\partial \alpha_i} = -\omega H_i \alpha_i. \quad (5)$$

Clearly, in contrast to the stress-like internal variables $\mathbf{Q}_k^{(j)}$ and Q_i being defined by Eqs. (4) and (5), the CAUCHY stress tensor $\boldsymbol{\sigma}$ as dual variable to $\boldsymbol{\epsilon}^e$ follows from the second law of thermodynamics for fully reversible processes.

For modeling damage accumulation, the effective stress concept is utilized which is based on the principle of strain equivalence. According to this principle, *the strain associated with the damaged state under the applied stress $\boldsymbol{\sigma}$ is equivalent to the strain associated with the undamaged state under the effective stress $\tilde{\boldsymbol{\sigma}}$* , cf. [13]. The undamaged state is defined by considering the virgin moduli \mathbb{C} , H_i and $H_k^{(j)}$ for vanishing damage ($D = 0$). Thus, the effective state variables ($\tilde{\bullet}$) are given by

$$\tilde{\boldsymbol{\sigma}} = \mathbb{C} : \tilde{\boldsymbol{\epsilon}}^e, \quad \tilde{\mathbf{Q}}_k^{(j)} = -H_k^{(j)} \tilde{\boldsymbol{\alpha}}_k^{(j)} \quad (j = 1, 2, 3), \quad \tilde{Q}_i = -H_i \tilde{\alpha}_i. \quad (6)$$

By enforcing the conditions of strain equivalence, i.e., $\tilde{\boldsymbol{\epsilon}}^e = \boldsymbol{\epsilon}^e$, $\tilde{\boldsymbol{\epsilon}}^p = \boldsymbol{\epsilon}^p$, $\tilde{\boldsymbol{\alpha}}_k^{(j)} = \boldsymbol{\alpha}_k^{(j)}$ and $\tilde{\alpha}_i = \alpha_i$, the relationships

$$\tilde{\boldsymbol{\sigma}} = \frac{\boldsymbol{\sigma}}{\omega}, \quad \tilde{\mathbf{Q}}_k^{(j)} = \frac{\mathbf{Q}_k^{(j)}}{\omega} \quad (j = 1, 2, 3), \quad \tilde{Q}_i = \frac{Q_i}{\omega}. \quad (7)$$

between the effective stress-like variables ($\tilde{\bullet}$) and their physical counterparts (\bullet) can be derived.

For deciding whether a considered loading step is dissipative or fully reversible, a yield function ϕ^p is introduced. It is assumed that this function depends solely on effective stresses. More precisely, a VON MISES yield function of the type

$$\phi^p = \sqrt{\frac{3}{2} \text{dev}(\tilde{\boldsymbol{\sigma}} - \tilde{\mathbf{Q}}_k) : \text{dev}(\tilde{\boldsymbol{\sigma}} - \tilde{\mathbf{Q}}_k) - (\tilde{Q}_i + Q_0^{eq})} \leq 0 \quad (8)$$

is adopted, where Q_0^{eq} represents the initial radius of the elastic domain and $\text{dev}(\bullet)$ is the deviatoric projector, i.e., $\text{dev}(\boldsymbol{\sigma}) = \boldsymbol{\sigma} - 1/3 \text{tr} \boldsymbol{\sigma} \mathbf{1}$. Hence, according to the effective stress concept, damage and elasto-plastic effects are uncoupled, i.e., the yield function is independent of D . However, a kinetic coupling still exists, since the damage evolution is affected by the plastic strain rate. This will be shown explicitly later.

The model is completed by suitable evolution equations. For providing enough flexibility even for non-linear kinematic hardening, the framework of *generalized standard media* is utilized here, cf. [14]. Within this framework, the evolution laws are derived from a plastic potential $\bar{\phi}^p$. Similar to [13, 14], $\bar{\phi}^p$ is assumed to be of the type

$$\bar{\phi}^p = \phi^p + \frac{Y^M}{M S_1 \omega (1 - D)^K} + \sum_{j=1}^3 \frac{B_k^{(j)}}{H_k^{(j)}} \frac{\tilde{\mathbf{Q}}_k^{(j)} : \tilde{\mathbf{Q}}_k^{(j)}}{2} + \frac{B_i}{H_i} \frac{\tilde{Q}_i^2}{2}. \quad (9)$$

Here, M , S_1 and K are material parameters describing the damage evolution and $B_k^{(j)}$ and B_i are material parameters controlling the saturation values of the hardening stresses according to ARMSTRONG-FREDERICK. Furthermore,

$$Y = -\rho \frac{\partial \Psi^{ep}}{\partial D} = \frac{\boldsymbol{\epsilon}^e : \mathbb{C} : \boldsymbol{\epsilon}^e}{2} + \sum_{j=1}^3 H_k^{(j)} \frac{\boldsymbol{\alpha}_k^{(j)} : \boldsymbol{\alpha}_k^{(j)}}{2} + H_i \frac{\alpha_i^2}{2} \quad (10)$$

is the energy release rate. Complying with the framework of generalized standard media (see [14]), the evolution laws are postulated as

$$\dot{\boldsymbol{\epsilon}}^p = \lambda^p \frac{\partial \bar{\phi}^p}{\partial \boldsymbol{\sigma}} = \lambda^p \frac{\partial \bar{\phi}^p}{\partial \boldsymbol{\sigma}} : \frac{\partial \boldsymbol{\sigma}}{\partial \boldsymbol{\sigma}} = \frac{\lambda^p \mathbf{n}}{\omega} = p \mathbf{n}, \quad (11)$$

$$\begin{aligned} \dot{\boldsymbol{\alpha}}_k^{(j)} &= \lambda^p \frac{\partial \bar{\phi}^p}{\partial \mathbf{Q}_k^{(j)}} = \lambda^p \frac{\partial \bar{\phi}^p}{\partial \tilde{\mathbf{Q}}_k^{(j)}} : \frac{\partial \tilde{\mathbf{Q}}_k^{(j)}}{\partial \mathbf{Q}_k^{(j)}} \quad (j = 1, 2, 3), \\ &= \frac{\lambda^p}{\omega} (-\mathbf{n} + \frac{B_k^{(j)}}{H_k^{(j)}} \tilde{\mathbf{Q}}_k^{(j)}) = -p (\mathbf{n} + B_k^{(j)} \boldsymbol{\alpha}_k^{(j)}), \end{aligned} \quad (12)$$

$$\begin{aligned} \dot{\alpha}_i &= \lambda^p \frac{\partial \bar{\phi}^p}{\partial Q_i} = \lambda^p \frac{\partial \bar{\phi}^p}{\partial \tilde{Q}_i} : \frac{\partial \tilde{Q}_i}{\partial Q_i} \\ &= \frac{\lambda^p}{\omega} (-1 + \frac{B_i}{H_i} \tilde{Q}_i) = -p (1 + B_i \alpha_i), \end{aligned} \quad (13)$$

$$\dot{D} = \lambda^p \frac{\partial \bar{\phi}^p}{\partial Y} = p \frac{Y^{M-1}}{S_1 (1-D)^K}. \quad (14)$$

Here, the definitions $p := \frac{\lambda^p}{\omega}$ and $\mathbf{n} := \frac{\partial \bar{\phi}^p}{\partial \boldsymbol{\sigma}}$ have been introduced. Hence, p equals the equivalent plastic strain rate, i.e.,

$$\sqrt{\frac{2}{3}} \dot{\boldsymbol{\epsilon}}^p : \dot{\boldsymbol{\epsilon}}^p = p. \quad (15)$$

The plastic multiplier $\lambda^p \geq 0$ fulfills the KUHN-TUCKER complementarity conditions

$$\lambda^p \geq 0, \quad \phi^p(\boldsymbol{\sigma}, \mathbf{Q}_k^{(j)}, Q_i) \leq 0 \quad \text{and} \quad \lambda^p \phi^p = 0 \quad (16)$$

as well as the consistency condition

$$\lambda^p \dot{\phi}^p = 0. \quad (17)$$

Considering $\dot{\phi}^p = 0$, together with Eqs. (11) to (13), the plastic multiplier p is derived as

$$p = \frac{\mathbf{n} : \mathbb{C} : \dot{\boldsymbol{\epsilon}}}{\mathbf{n} : \mathbb{C} : \mathbf{n} + \sum_{j=1}^3 H_k^{(j)} (\frac{3}{2} + B_k^{(j)} \mathbf{n} : \boldsymbol{\alpha}_k^{(j)}) + H_i (1 + B_i \alpha_i)}. \quad (18)$$

It can be proved in a straightforward manner that the dissipation

$$\mathcal{D} = \boldsymbol{\sigma} : \dot{\boldsymbol{\epsilon}} - \rho \dot{\Psi}^{ep} = \boldsymbol{\sigma} : \dot{\boldsymbol{\epsilon}}^p + \sum_{j=1}^3 \mathbf{Q}_k^{(j)} : \dot{\boldsymbol{\alpha}}_k^{(j)} + Q_i \dot{\alpha}_i + Y \dot{D} \geq 0, \quad (19)$$

as predicted by the discussed model, is non-negative and thus, the second law of thermodynamics is indeed fulfilled. This is a direct consequence, of the convexity of the plastic potential $\bar{\phi}^p$, cf. [14].

4.2. The brittle damage model

According to Sections 2 and 3, a quasi-brittle-type damage mechanism can also be observed in Al2024. Therefore, the ductile damage model as discussed in the previous subsection is supplemented by an additional brittle-type damage model here. For deciding whether this additional model is active or not, a novel damage indicator function is proposed (analogous to a yield function). It reads

$$\phi^d = \frac{|Y^N - \Gamma|}{S_2} - (Q_d + Q_{d0}) \leq 0. \quad (20)$$

Here, $(Q_d + Q_{d0})$ defines a threshold with a constant value Q_{d0} and a variable value Q_d . Γ is the so-called *shift tensor* which has been introduced for describing cyclic loading effects (similar to ARMSTRONG-FREDERICK-type hardening), Y is the energy release rate (see Eq. (10)) and N is a material parameter. Assuming the internal variables governing ductile and brittle damage to be uncoupled, an additive form of the HELMHOLTZ energy is assumed. More precisely,

$$\rho \Psi^d = \omega Y + H_d \frac{\alpha_d^2}{2} + H_\Gamma \frac{\alpha_\Gamma^2}{2}. \quad (21)$$

α_Γ and α_d are the strain-like variables dual to the energy-like variables Γ and Q_d , respectively. Both sets of variables are related by the state equations as

$$\Gamma = -\rho \frac{\partial \Psi^d}{\partial \alpha_\Gamma} = -H_\Gamma \alpha_\Gamma \quad \text{and} \quad Q_d = -\rho \frac{\partial \Psi^d}{\partial \alpha_d} = -H_d \alpha_d. \quad (22)$$

Accordingly, H_Γ and H_d can be interpreted as hardening parameters.

Fully analogous to the elasto-plastic model presented before, the novel approach discussed here is further elaborated by postulating suitable evolution equations. For that purpose, the (convex) damage potential

$$\bar{\phi}^d = \phi^d + \frac{B_d}{H_d} \frac{Q_d^2}{2} + \frac{B_\Gamma}{H_\Gamma} \frac{\Gamma^2}{2} \quad (23)$$

is introduced. Here, B_Γ and B_d are material parameters which have a similar meaning as the saturation parameters B_i or $B_k^{(j)}$ in the elasto-plastic rate problem. Based on Eq. (23), the evolution equations are derived by applying the framework of generalized standard media (see [14]), i.e.,

$$\dot{\alpha}_\Gamma = \lambda^d \frac{\partial \bar{\phi}^d}{\partial \Gamma} = -\lambda^d \left(\frac{\text{sign}(Y^N - \Gamma)}{S_2} + B_\Gamma \alpha_\Gamma \right), \quad (24)$$

$$\dot{\alpha}_d = \lambda^d \frac{\partial \bar{\phi}^d}{\partial Q_d} = -\lambda^d (1 + B_d \alpha_d), \quad (25)$$

$$\dot{D} = \lambda^d \frac{\partial \bar{\phi}^d}{\partial Y} = \lambda^d \frac{\text{sign}(Y^N - \Gamma)}{S_2} N Y^{N-1}. \quad (26)$$

The multiplier $\lambda^d \geq 0$ fulfills the KUHN-TUCKER complementarity conditions

$$\lambda^d \geq 0, \quad \phi^d(Y, \Gamma, Q_d) \leq 0 \quad \text{and} \quad \lambda^d \phi^d = 0, \quad (27)$$

together with the consistency requirement

$$\lambda^d \dot{\phi}^d = 0. \quad (28)$$

Considering $\dot{\phi}^d = 0$, the damage consistency parameter can be obtained as

$$\lambda^d = \frac{\frac{\text{sign}(Y^N - \Gamma)}{S_2} N Y^{N-1} \dot{Y}}{B_\Gamma \frac{\text{sign}(Y^N - \Gamma)}{S_2} (\Gamma_\infty - \Gamma) + B_d (Q_{d\infty} - Q_d)} \quad (29)$$

where the limit stresses $\Gamma_\infty = \frac{H_\Gamma \text{sign}(Y^N - \Gamma)}{S_2 B_\Gamma}$ and $Q_{d\infty} = \frac{H_d}{B_d}$ have been introduced by assuming the limit values

$$\frac{\text{sign}(Y^N - \Gamma)}{S_2} + B_\Gamma \alpha_{\Gamma_\infty} = 0 \quad \text{and} \quad 1 + B_d \alpha_{d\infty} = 0 \quad (30)$$

in combination with Eqs. (22). A careful analysis of the the damage rate

$$\dot{D} = \left(\frac{N}{S_2}\right)^2 \frac{Y^{2(N-1)} \dot{Y}}{B_\Gamma \frac{\text{sign}(Y^N - \Gamma)}{S_2} (\Gamma_\infty - \Gamma) + B_d (Q_{d\infty} - Q_d)} \quad (31)$$

reveals that Γ_∞ and $Q_{d\infty}$ define an implicit threshold at which the damage rate accelerates significantly. In contrast to \dot{D} it can be shown that the evolution of Γ or Q_d is not affected by the limit values Γ_∞ or $Q_{d\infty}$. This is in sharp contrast to the elasto-plastic rate problem where B_i or $B_k^{(j)}$ actually define the saturation values for the hardening stresses.

For the sake of completeness, the dissipation predicted by the model is given as well. It reads

$$D = \Gamma \dot{\alpha}_\Gamma + Q_d \dot{\alpha}_d + Y \dot{D} \geq 0. \quad (32)$$

As mentioned before, since the evolution equations have been derived from a convex potential, i.e., within the framework of generalized standard solids, the second law of thermodynamics is automatically fulfilled.

4.3. The coupled ductile-brittle damage model

Finally, both models as outlined in the previous two sections are integrated into one ductile-brittle damage model. In line with the previous subsection, the HELMHOLTZ energy of that model is assumed to be of the type

$$\rho \Psi = \omega \left(\frac{\boldsymbol{\epsilon}^e : \mathbb{C} : \boldsymbol{\epsilon}^e}{2} + \sum_{j=1}^3 H_k^{(j)} \frac{\boldsymbol{\alpha}_k^{(j)} : \boldsymbol{\alpha}_k^{(j)}}{2} + H_i \frac{\alpha_i^2}{2} \right) + H_d \frac{\alpha_d^2}{2} + H_\Gamma \frac{\alpha_\Gamma^2}{2}. \quad (33)$$

While the elasto-plastic part of the model is governed by the yield function (8), together with the evolution equations implied by the plastic potential (9), the brittle damage evolution is driven by Eqs. (20) and (21). The total material degradation D is assumed to be a superposition of the plastic part D^d and the brittle part D^b . More precisely, by introducing the composition factor $\gamma^d = (1 - \gamma^b) \in [0, 1]$ fulfilling the compatibility equation $\gamma^d + \gamma^b = 1$, the coupling of both models is provided by

$$\omega = (1 - \gamma^d D^d - \gamma^b D^b). \quad (34)$$

This choice leads to an additive decomposition of the energy release into a ductile and a brittle part, i.e.,

$$Y^d = \gamma^d \left(\frac{\boldsymbol{\epsilon}^e : \mathbb{C} : \boldsymbol{\epsilon}^e}{2} + \sum_{j=1}^3 H_k^{(j)} \frac{\boldsymbol{\alpha}_k^{(j)} : \boldsymbol{\alpha}_k^{(j)}}{2} + H_i \frac{\alpha_i^2}{2} \right), \quad (35)$$

$$Y^b = \gamma^b \left(\frac{\boldsymbol{\epsilon}^e : \mathbb{C} : \boldsymbol{\epsilon}^e}{2} + \sum_{j=1}^3 H_k^{(j)} \frac{\boldsymbol{\alpha}_k^{(j)} : \boldsymbol{\alpha}_k^{(j)}}{2} + H_i \frac{\alpha_i^2}{2} \right) \quad (36)$$

which in turn, yields the additive structure of the damage evolution $D = \gamma^d D^d + \gamma^b D^b \in [0, D_{crit}]$ with

$$\dot{D}^d = p \frac{Y^{dM-1}}{S_1 (1 - D^d)^K}, \quad D^d \in [0, D_{crit}^d], \quad (37)$$

$$\dot{D}^b = \lambda^d \frac{\text{sign}(Y^{bN} - \Gamma)}{S_2} N Y^{bN-1}, \quad D^b \in [0, D_{crit}^b]. \quad (38)$$

It can be shown in a relatively straightforward manner that this additive decomposition is also fulfilled for the dissipation, i.e.,

$$-D \dot{Y} = -\lambda^p \frac{\partial \bar{\phi}^p}{\partial Y^d} Y^d - \lambda^d \frac{\partial \bar{\phi}^d}{\partial Y^b} Y^b. \quad (39)$$

Since each submodel (ductile damage and brittle damage) is thermodynamically consistent, i.e., obeys the second law of thermodynamics, the resulting model is indeed physically sound as well and the dissipation inequality is thus fulfilled. To guarantee a positive damage evolution for brittle damage, damage growth is considered for a half-cycle only, i.e., in case of a positive sign of $(Y^{bN} - \Gamma)$.

5. Mechanical testing

Two types of specimens were tested. A so-called *Damage Low Cycle specimen* (DLC, smooth round bar) was designed for tension-compression tests showing a stress state close to the uni-axial one. Additionally, circumferential Round Notch Bars (RNB) with various notch radii were designed to achieve a variation of the stress state in the middle cross section of the specimens. For detailed information, refer to [10]. All specimens were cut from the same plate of Al2024-T351 in S- (small transversal)-direction and they were mechanically treated with a turning machine. The length of the specimens is equal to the thickness of the plate. Hence, the effective measuring length is associated with the mid-plane of the plate under investigation. Since scratches at the surface of the specimens could result in stress concentrations which affect the lifetime, the surfaces of the specimens were ground and mechanically polished in the direction of loading.

All experiments were conducted in a 60 kN servo-hydraulic testing machine. Specially designed gripping of the testing setup and clamping threads of the specimens allow for tension-compression reversal loading. The cyclic tests in all cases were performed displacement-controlled. The displacements were measured using an extensometer attached to the working distances in the case of the DLC-specimen as shown in Fig. 7, while the extensometer was attached to specially manufactured



Figure 7: Experimental test specimens. a) DLC (Damage Low Cycle specimen); (b) RNB (Round Notch Bars) $R = 10\text{mm}$; (c) RNB $R = 2\text{mm}$

grooves in case of the RNB-specimens, see Fig. 7. A symmetric cycle ($R=-1$) based on a triangular wave shape was imposed with various displacement amplitudes Δl . The time period was not varied ($T=100\text{s}$). All tests were conducted until complete failure (separation of the specimens into two parts). Time-force-displacement responses during the tests were recorded with a digital acquisition device. The gauge length of the smooth round bars (DLC) was 10 mm and that of the RNB 25 mm.

The experimental results (number of cycles) for different strain ranges are presented in Fig. 8, where $\Delta\epsilon^p$ represents the strain amplitude for stabilized conditions, i.e., when the peak stress remains constant from cycle to cycle.

6. Parameter identification

In the present section, the parameter identification strategy is outlined. First, the brittle damage law is calibrated to small fatigue crack growth considering Al2024 alloys. Then, the plastic moduli are defined by matching the experimentally observed elasto-plastic hysteresis curve for a medium strain range. For defining damage initiation, a reasonable activation criterion is presented which is finally calibrated to Al2024 by comparing the experimentally observed and numerically simulated number of cycles. For this purpose, the time of damage initiation, as observed in the experiments, has been identified by the moment when the peak stress starts decreasing. Finally, the softening process is described by the proposed ductile-brittle damage law. Its material parameters are found by comparing the experimentally observed and numerically simulated lifetimes. As optimization strategy, an iterative approach has been used according to NELDER MEAD, cf. [16]. The parameter identification has been done for a one-dimensional uni-axial tension-compression test.

6.1. Calibration of the brittle damage model to Al2024

The novel brittle damage law discussed in the present paper is used for describing the damage process of fatigue crack growth. A well known model which describes fatigue crack growth for rather long cracks was proposed by PARIS [17]. It reads

$$\frac{da}{dN} = C (\Delta K)^\eta, \quad (40)$$

where C and η are material parameters. ΔK is the stress intensity factor range which can be computed by $\Delta K = K_{max} - K_{min} = K_{max} = K$, if $K_{min} = 0$ is assumed (cyclic loading with $R = 0$). In general, the rate of small crack growth can be different to

that of long crack growth. However, according to [1], the small crack growth rate can be reasonably approximated by a model for long cracks. Consequently, PARIS' law is also considered here. For Al2024, the material parameters for the PARIS law are documented in [19]. For two different geometrical scaling factors, two distinct values of η , 2.73 and 3.24, are reported. In what follows, an average value of $\eta = 3.0$ is considered. Regarding the stress intensity factor, it can be computed in terms of the energy release rate (see [13], p. 71). More precisely,

$$K = \sqrt{EG} = \sqrt{EY}, \quad (41)$$

where G is GRIFFITH'S energy release. Clearly, in case of crack growth, it equals the energy release rate Y .

For relating PARIS law to the brittle damage model elaborated in the previous subsection, the time derivative of Eq. (40), evaluated over one cycle, is computed. It gives

$$\dot{a} = \eta C K^{\eta-1} \dot{K}. \quad (42)$$

Consequently, by inserting Eq. (41) into Eq. (42), a relation between the energy release rate and the crack growth of the type

$$\dot{a} = \eta C (\sqrt{EY})^{\eta-1} \frac{\sqrt{E}}{2} Y^{-1/2} \dot{Y} = \bar{C} Y^{\eta/2-1} \dot{Y}, \quad (43)$$

can be derived. Here, \bar{C} is a material constant. By further assuming $\dot{D} \sim \dot{a}$, the proposed brittle damage is related to PARIS law by

$$\dot{D} \sim Y^{2(N-1)} \dot{Y}. \quad (44)$$

Accordingly, a comparison of both models yields the material parameter $N = 1.25$.

Considering the damage evolution rate (31), S_2 can be neglected. Here, the admissible choice $S_2=N=1.25$ is made. For the sake of further simplification and to reduce the unknown material parameters, the variable damage threshold value Q_d will be neglected in our numerical simulations, i.e., an evolving damage threshold will be modelled by means of the shift tensor Γ only. Summarizing the aforementioned assumptions and simplifications yields finally

$$\dot{D} = \frac{N \sqrt{Y^b} \dot{Y}^b}{B_\Gamma (\Gamma_\infty - \Gamma)} = \frac{1.25 \sqrt{Y^b} \dot{Y}^b}{B_\Gamma (\Gamma_\infty - \Gamma)}. \quad (45)$$

Here, $(\bullet)_\infty$ denotes the limit values of the respective variable (\bullet) .

For computing the constant damage threshold value Q_{d0} (initial threshold), the endurance limit is considered in general.

Specimen / Δl [mm]	$\Delta\epsilon$	$\Delta\epsilon^p$	N_D^{exp}	N_E^{exp}	N_R^{exp}
ML / 0.8	0.08	0.0664	1	-	1
SR-1 / 0.4	0.04	0.0247	9	1	10
SR-2 / 0.3	0.03	0.0153	27	3	30
SR-3 / 0.25	0.025	0.0115	48	5	53
SR-4 / 0.2	0.02	0.0063	116	22	138
SR-5 / 0.18	0.018	0.00487	145	21	166

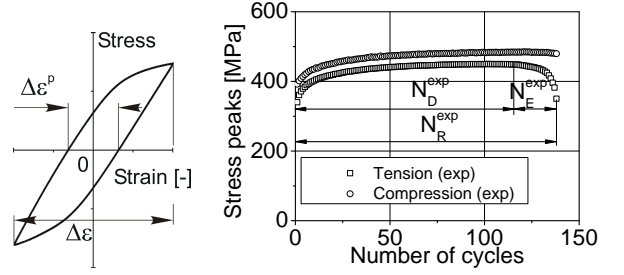


Figure 8: (a) Experimental results for smooth round bars (abbreviation DLC or SR); S-loading direction. Sketches for definitions of (b) cyclic strain range; (c) N_D^{exp} , N_E^{exp} and N_R^{exp}

However, for aluminum such a clear endurance limit does not exist. Given that the endurance limit can be set for a number of cycles at fracture $N_f \sim 10^7$ - 10^8 , the CAUCHY stress lies in the range $\sigma_f \sim 50$ - 75 MPa. Knowing σ_f and assuming instantaneous damage initiation in the first cycle, i.e.,

$$\phi^d = \frac{Y^{bN}}{N} - Q_{d0} = 0 \quad (46)$$

Q_{d0} can be computed from

$$Q_{d0} = \frac{\left(\gamma^b \frac{\sigma_f^2}{2E}\right)^N}{N}. \quad (47)$$

Here, a purely elastic material state has been considered. For an average value $\sigma_f = 62.5$ MPa, Q_{d0} is computed as 0.009636272 $(\text{MJ}/\text{m}^3)^N$ ($\gamma^b = 1.0$, $E = 67000.0$ MPa, $N = 1.25$).

6.2. The approximation of the elasto-plastic hysteresis curve

To permit a good approximation of the plastic hysteresis curve, three back stress tensors are superposed (see [14], p. 234). In particular, the introduction of a linear kinematic hardening rule (third back stress tensor) improves the description of strain ratcheting, i.e., the growth of permanent strains from cycle to cycle. A single ARMSTRONG-FREDERICK rule usually overpredicts the ratcheting effect. The linear rule defines in particular the slope of the hysteresis curve at the point of strain reversal. The set of plastic parameters has been found by matching the experimentally obtained and numerically simulated elasto-plastic hysteresis curves for a medium strain range of $\Delta\epsilon = 0.025$ with 53 number of cycles to fracture, see Tabs. 3 (consider a factor $\frac{2}{3}$ for $H_k^{(j)}$ in the three-dimensional case). In Fig. 9, the stress-

Table 3: Computed material parameters characterizing the elasto-plastic response (DLC specimen, $\Delta\epsilon = 0.025$)

$H_k^{(1)}$ (MPa)	$H_k^{(2)}$ (MPa)	$H_k^{(3)}$ (MPa)	H_i (MPa)	E (MPa)	
180000.0	5000.0	6010.0	1026.496	67000.0	
$B_k^{(1)}$	$B_k^{(2)}$	$B_k^{(3)}$	B_i	Q_0^{eq} (MPa)	ν
3050.0	20.0	0.0	6.8433	225.0	0.3

strain diagrams obtained experimentally and those simulated numerically are presented for the first four loading cycles. The approximation is not completely in line with the experimental data, but reproduces the cyclic behavior quite satisfactorily.

6.3. The damage initiation phase

The instant of damage initiation is related to the amount of energy expended on the incubation of defects. Hence, it is correlated to the storage of internal plastic energy. In line with [4], a modified energy functional is considered here. More precisely, the energy expended on the incubation of defects related to isotropic hardening is assumed to be of the type

$$\hat{w}_s = \int_0^t R_\infty (1 - e^{-br}) \left(\frac{A}{m}\right) r^{\frac{1-m}{m}} \dot{r} dt. \quad (48)$$

Here, A and m are scaling parameters. The same model has been used in our earlier works [10] for defining damage initiation. r is the accumulated plastic strain (see [15], p. 28), while R_∞ and b are related to an exponential decay rule. Since in the current setting an ARMSTRONG-FREDERICK rule is used, which is defined by H_i and B_i , both parameter sets have to be consistent.

Evidently, the stored energy corresponding to the back stress tensor affects damage initiation as well. However, since the first back stress saturates very fast, while the last back stress would lead to a too large energy (linear hardening), only the second back stress is considered in what follows. Thus, the energy expended on the incubation of defects is approximated by

$$w_s = \hat{w}_s + \frac{H_k^{(2)}}{2} (\alpha_k^{(2)} : \alpha_k^{(2)}) \quad (49)$$

and damage initiation is assumed, if

$$w_s \geq w_D \quad (50)$$

with w_D being a threshold value.

In summary, defining damage initiation requires to determine the set of material parameters $[A, m, w_D]$.

6.3.1. Parameter identification strategy

In order to determine a set of material parameters A , m and w_D , the objective function

$$\{A, m, w_D\}^* = \arg \min_{\{A, m, w_D\}} \left(\sum_1^n \text{abs}(\log N_{D,i}^{\text{exp}} - \log N_{D,i}^{\text{sim}}) \right). \quad (51)$$

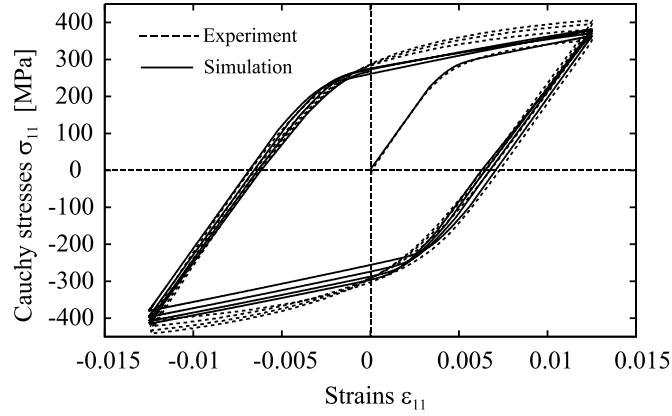


Figure 9: Elasto-plastic hysteresis; Experimental data and simulations for a strain range of $\Delta\epsilon=0.025$

is minimized. Here, $N_{D,i}^{\text{exp}}$ are the experimentally observed cycles, $N_{D,i}^{\text{sim}}$ are the numerically simulated counterparts and n is the number of experiments with different strain ranges (see Fig. 8; $n=5$; SR-1 to SR-5).

The final material parameters are summarized in Tab. 4. Within the computations, $R_{\infty}=150.0$ MPa and $b=6.82$ have been

Table 4: Optimized parameters for defining damage initiation

m	A	w_D (MJ/m ³)
4.8972	0.009824	0.66295

used for the exponential decay rule. Using R_{∞} and b , nearly 96.6% saturation of cyclic hardening is reached for an accumulated plastic strain of $\sum_{N_{\text{cycles}}} \Delta\epsilon^p=0.5$. The consistent material parameters H_i and B_i are defined according to Tab. 3.

6.4. The coupled damage model

Although a ductile damage model similar to that proposed in the present paper has already been calibrated and applied in our analyses [10, 26], all material parameters associated with the ductile damage model are re-calibrated here. Hence, by assuming $K = 0$, M and S_1 have to be determined. Adding the till now unknown parameters B_{Γ} and H_{Γ} for the brittle damage model and the composition factor γ^d , the parameter set to be defined is $[M, S_1, B_{\Gamma}, H_{\Gamma}, \gamma^d]$. A mesoscopic crack is assumed, if the critical values of the damage variables $D_{\text{crit}}^{b,d} = D_{\text{crit}}=0.23$ are reached.

6.4.1. The crack closure effect

For the modeling of crack closure, a prefactor of 0.2 is considered for the ductile composition factor γ^d in the compressive part of a cycle (if $\text{tr}(\boldsymbol{\sigma}) < 0$). For the brittle damage contribution, no such distinction is made. However, the effect of crack closure is considered also for the brittle damage part, since damage evolves in a half-cycle only, i.e., if $\text{sign}\left(\frac{\gamma^d N - \Gamma}{S_2}\right) > 0$.

6.4.2. Parameter identification strategy

The parameter identification was carried out in three steps. Within each of those the minimization problem

$$\{\dots\}^* = \arg \min_{\{\dots\}} \left(\sum_1^n \text{abs}(\log N_{R,i}^{\text{exp}} - \log N_{R,i}^{\text{sim}}) \right), \quad (52)$$

was considered ($n=5$, cf. Eq. (51)). At first, the ductile damage model was calibrated (for finding M and S_1). Subsequently, the same procedure was applied to the determination of the brittle damage parameters B_{Γ} and H_{Γ} . Finally, a fully coupled analysis yielded the composition factor γ^d . The final material parameters are presented in Tab. 5.

Table 5: Remaining material parameters for the combined ductile-brittle damage model law

M	S_1	B_{Γ}	H_{Γ}	γ^d
1.6	1.544	0.992	121.5	0.86

7. Numerical example of a smooth round bar (DLC-specimen)

The prediction capability of the novel ductile-brittle damage model is demonstrated here by re-analyzing a smooth round bar (SR), see Fig. 8. Its middle-section has been discretized by the finite element mesh shown in Fig. 10. Due to symmetry, only one quarter of the structure has been discretized. For a detailed description of the specimen dimensions, refer to [10]. The computation was done displacement-controlled. The right boundary at the free end is slightly conical to force localization at the bottom right corner of the structure. The fully three-dimensional CDM model as presented in the previous sections has been implemented into a UMAT-routine in ABAQUS. To improve the convergence of the NEWTON iteration scheme at the material point level, a line-search according to [18] has been applied. The same technique was also employed at the global level (equilibrium iteration). Mesocrack initiation was assumed

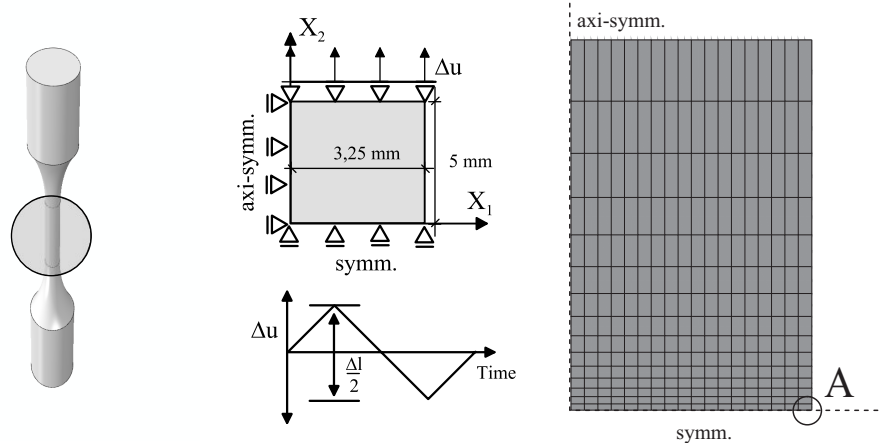


Figure 10: Sketch of the DLC-specimen, loading conditions and finite element discretization

Table 6: Numerically simulated number of cycles N_D^{sim} and N_R^{sim} and error with respect to N_R^{exp} ("SR-X" abbreviation according to Tab. 8)

Type	1-D		3-D	
	N_D^{sim}	N_R^{sim}	N_D^{sim}	N_R^{sim}
SR-1	9.25	12.11/+21.1%	8.7	11.2/+12%
SR-2	29.75	34.06/+11.9%	29.27	33.7/+12.3%
SR-3	52.25	58.25/+9.0%	52.2	59.0/+11.3%
SR-4	101.25	112.04/-18.8%	101.7	113.0/-18.1%
SR-5	144.24	159.13/-4.1%	145.7	161.0/-3.0%

at the moment at which the critical damage threshold of 0.23 was reached. As expected, this threshold was reached first at the local integration point near the middle-section at the right boundary of the structure (point A).

The results are presented in Tab. 6 where also the estimated number of cycles for the one-dimensional case (as optimized during the parameter identification) are included. As can be seen, the numerical results for the one-dimensional and the three-dimensional case are nearly identical. Only for SR-1, the fully three-dimensional computation gives a slightly better prediction for N_R^{sim} . Accordingly, the use of the fully coupled ductile-brittle damage model leads to a prediction of lifetimes in good agreement with those experimentally observed. A more careful analysis reveals that the numerical simulation could be further improved by modifying the damage activation criterion (compare N_D^{sim} to Fig. 8) since an error in N_D^{sim} clearly affects also the prediction for N_R^{sim} . According to Fig. 11, the portion of the plastic strain energy related to kinematic hardening plays a much greater role for SR-1, in comparison to SR-5 where the cyclic portion of the w_s -curve is negligible.

In Figs. 12 and 13, the total damage accumulation as well as its defining single parts are plotted. As evident, the brittle damage part plays only a minor role for SR-1, while its effect is more pronounced for SR-5. This would imply that small fatigue crack growth is more relevant for large numbers of cycles, espe-

cially for HCF. Furthermore, as can be seen in Figs. 12 and 13, the fracture criterion for D^d is reached first, while the complete damage variable is still below its threshold. By comparing the numerical results to the experimental observations, it can be concluded that the brittle damage part is slightly underestimated for a smaller number of cycles. To increase its influence, different modifications are possible. The probably most promising one, which will be considered in future, is a variable composition factor.

The peak stresses as a function of the number of loading cycles are shown in Fig. 14. As can be observed, the maximum stresses in tension are smaller than those in compression. This effect, which can also be observed in experiment, is a direct consequence of the crack closure effect.

8. Conclusion

In the present paper, a coupled isotropic ductile-brittle damage model suitable for the numerical analysis of LCF in high-strength aluminum alloys has been proposed. This model is a result of research activities in different areas ranging from experiments and characterization to the numerical implementation as well as the final calibration of the material parameters. For modeling ductile damage evolution, an approach similar to that proposed by LEMAITRE (see [13]) has been utilized, while for brittle damage accumulation a novel model for small fatigue crack growth has been proposed. Based on these models, a fully coupled approach approximating a quasi-brittle damage evolution was advocated. It has been applied to the prediction of lifetimes at high stress levels (LCF) in the S-direction of an aluminum 2024 alloy. Since the resulting model shows a large number of material parameters, an efficient, hybrid parameter identification strategy has been discussed. Within this strategy, as many parameters as possible have been determined a priori by exploiting analogies to established theories (like PARIS' law), while the remaining free unknowns were computed by solving an optimization problem. Comparisons between the experimentally obtained lifetimes and their numerically simulated counterparts revealed that the proposed model is very promising for

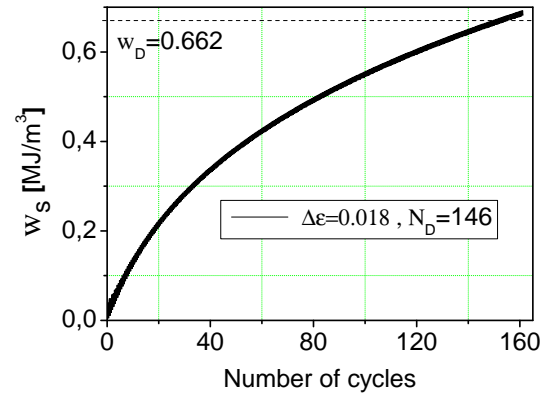
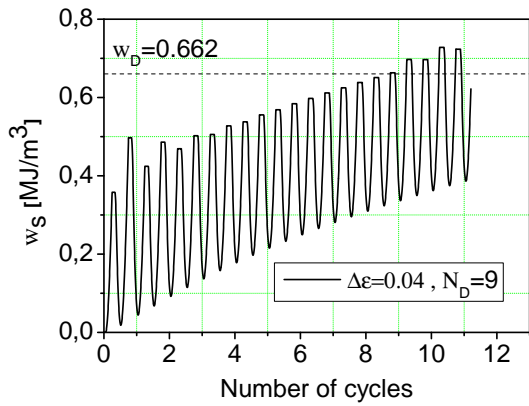


Figure 11: Damage activation criterion for two different strain amplitudes in point A (a) SR-1; (b) SR-5; see Tab. 8

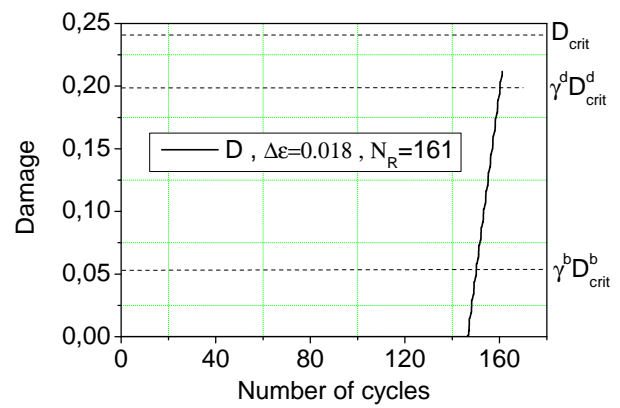
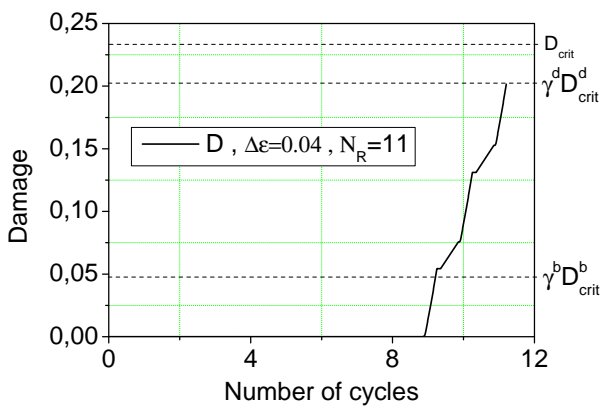


Figure 12: Complete damage variable for two different strain amplitudes in point A (a) SR-1; (b) SR-5; see Tab. 8

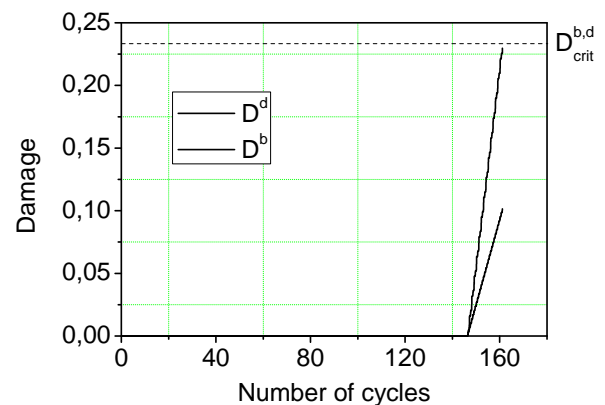
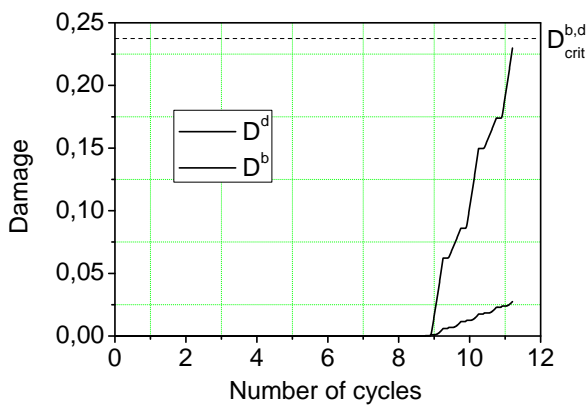


Figure 13: Ductile and brittle damage variables for two different strain amplitudes in point A (a) SR-1; (b) SR-5; see Tab. 8

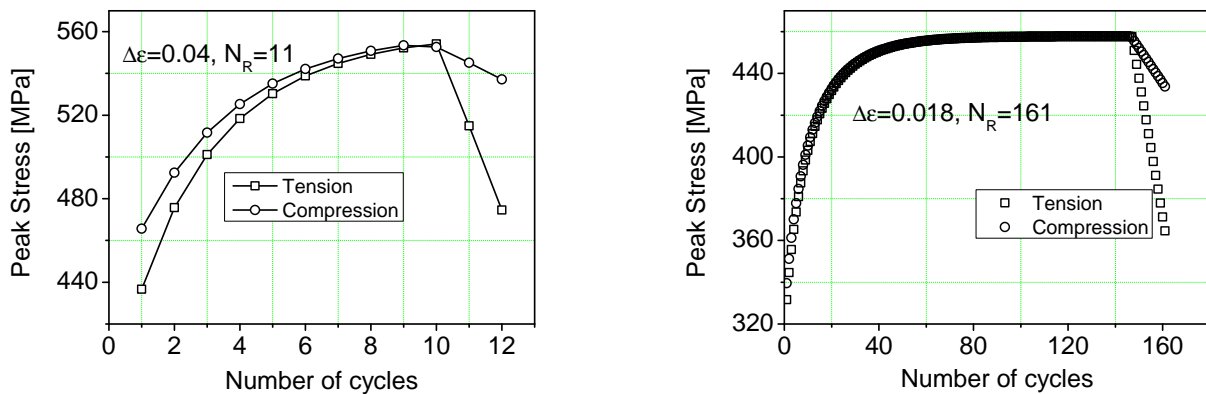


Figure 14: Maximum CAUCHY stresses for two different strain amplitudes in point A (a) SR-1; (b) SR-5; see Tab. 8

the application to LCF.

Although the predicted lifetimes are in good agreement with the respective experiments, the relative contribution of the brittle damage model is slightly underestimated for a smaller number of cycles. Therefore, future work will focus on a variable composition factor γ^d and improved threshold values for the brittle damage law.

References

- [1] ASM-Handbook, 1996. Fatigue and Fracture, Volume 19. ASM, Materials Park.
- [2] Beremin, F. M., 1981. Cavity formation from inclusions in ductile fracture of a508 steel. Metall. Trans. A 12A, 723–731.
- [3] Chabanet, O., Steglich, D., Besson, J., Heitmann, V., Hellmann, D., Brocks, W., 2003. Predicting crack growth resistance of aluminium sheets. Comput. Mater. Sci. 26, 1–12.
- [4] Chrysochoos, A., 1987. A Dissipation et blocage d'énergie lors d'un ecrouissage en traction simple. Ph.D. thesis, Paris, France.
- [5] Cordebois, J., Sidoroff, F., 1979. Damage induced elastic anisotropy, in: Mechanical Behavior of Anisotropic Solids, ed. Boehler, Nijhoff Edition. Boston, pp. 761–774.
- [6] de Hass, M., De Hosson, J., 2001. Grain boundary segregation and precipitation in aluminium alloys. Scripta Mater 44, 281–286.
- [7] Grammenoudis, P., Reckwerth, D., Tsakmakis, C., 2009. Continuum Damage Models based on Energy Equivalence: Part I - Isotropic Material Response. International Journal of Damage Mechanics 18 (No.1), 31–64.
- [8] Gurson, A., 1977. Continuum theory of ductile rupture by void nucleation and growth: Part I - Yield criteria and flow rules for porous ductile media. Journal of Engineering Materials and Technology January, 2–15.
- [9] Kachanov, L., 1958. Time of the Rupture Process under Creep Conditions. Isv. Akad. Nauk. SSR. Otd Tekh. Nauk. 8, 26–31.
- [10] Khan, S., Vyshnevskyy, A., Mosler, J., 2010. Low cycle lifetime assessment of Al2024 alloy. Int J Fatigue in press, –.
- [11] Kintzel, O., 2006. Modeling of elasto-plastic material behavior and ductile micropore damage of metallic materials at large deformations. Ph.D. thesis, Ruhr-University Bochum, Germany. Download at: <http://www-brs.uni-bochum.de/netahtml/HSS/Diss/KintzelOlafE>.
- [12] Lassance, D., Fabregue, D., Delannay, F., Pardoën, T., 2007. Micromechanics of room and high temperature fracture in 6xxx al alloys. Prog. Mater. Sci., 62–129.
- [13] Lemaitre, J., 1992. A course on damage mechanics. Springer, Berlin.
- [14] Lemaitre, J., Chaboche, J.-L., 1994. Mechanics of Solid Materials. Cambridge University Press.
- [15] Lemaitre, J., Desmorat, R., 2005. Engineering damage mechanics. Springer, Berlin.
- [16] Neadler, J., Mead, R., 1965. A simplex method for function minimization. Computer J. 7, 308–313.
- [17] Paris, P., Gomez, M., Anderson, W., 1961. A Rational Analytic Theory of Fatigue. The Trend in Engineering 13, 9–14.
- [18] Pérez-Foguet, A., Armero, F., 2002. On the formulation of closest-point projection algorithms in elasto-plasticity - Part ii: Globally convergent schemes. International Journal for numerical Methods in Engineering 53, 331–374.
- [19] Pieri, R., Sinclair, G., 1994. On the effects of scaling on the Paris law. Int J Fracture 68, R3–R8.
- [20] Quan, G., Heerens, J., Brocks, W., 2004. Distribution Characteristics of Constituent Particles in Thick Plate of 2024Al-T351. Prakt Metallograph 40, 304–313.
- [21] Rice, J., Tracey, D., 1969. On the Ductile Enlargement of Voids in Triaxial Stress Fields. J Mech Phys Solid 17, 201–217.
- [22] Rousselier, G., 1981. Finite deformation constitutive relations including ductile fracture damage, in: Three-Dimensional Constitutive Relations and Ductile Fracture Edition. North-Holland Publ. Comp., pp. 331–355.
- [23] Steglich, D., Brocks, W., Heerens, J., Pardoën, T., 2008. Anisotropic ductile fracture of Al alloys. Eng Fract Mech 75, 3692–3706.
- [24] Tvergaard, V., Needleman, A., 1984. Analysis of the cup-cone fracture in a round tensile bar. Acta Metall. 32, 157–169.
- [25] Verhoosel, C., Remmers, J., Miguel, A. G., de Borst, R., 2010. Computational homogenization for adhesive and cohesive failure in quasi-brittle solids. International Journal for numerical Methods in Engineering in press, –.
- [26] Vyshnevskyy, A., Khan, S., Mosler, J., 2009. An investigation on low cycle lifetime of Al2024 alloys. J Key Engng Mater 417-418, 289–292.